Journal of Applied Sciences and Nanotechnology

Journal homepage: jasn.uotechnology.edu.iq

Manufacturing of CuO@ZnO Nanoparticles Core-Shell for Enhancing Electrical Properties and Spectral Responsivity of Photodetectors

[1]Salah M. Abdul Aziz*, [2]Uday M. Nayef, [2]Mohammed Rasheed

[1]Sumer University-Department of Science, Dhi Qar, Iraq
[2]Department of Applied Sciences, University of Technology - Iraq, Iraq

A R T I C L E I N F O

Article history:
Received: September, 03, 2024
Accepted: November, 16, 2024
Available online: December, 10, 2024

Keywords:
CuO@ZnO core-shell,
Laser ablation,
Porous silicon,
Colloidal solution,
Photodetectors

Corresponding Author:
Salah M. Abdul Aziz
salahmhdi76@gmail.com

A B S T R A C T

Zinc oxide nanoparticles (ZnO NPs), copper oxide nanoparticles (CuO NPs) and CuO@ZnO NPs as a colloidal core-shell solution were synthesized by laser ablation. A Nd:YAG laser with an energy of 700 mJ, a wavelength of 1064 nm and 200 pulses was used for the ablation process. The colloidal solution was deposited on porous silicon (PSi) using the drop-casting method. The PSi substrates were prepared by photoelectrochemical etching (PECE) on n-type (111) silicon wafers. The study investigated the influence on the electrical, optical, morphological and structural properties of the CuO NPs and ZnO NPs samples when they were converted into a core-shell, specifically for their use in photodetector applications. XRD analysis revealed the presence of CuO, ZnO and CuO@ZnO by diffraction peaks at different angles. According to the SEM images, the nanoparticles show randomly distributed spherical grains, while PSi exhibits a sponge-like structure. The core-shell shape is confirmed by TEM images, which show a dark inner region consisting of CuO NPs and a much lighter outer region consisting of the ZnO nanoshell. The optical properties of the CuO@ZnO NPs were investigated and a minimum energy gap of 2.8 eV was found. The CuO@ZnO NPs/PSi/n-Si photodetector showed improved current-voltage (J-V) characteristics, rectifying properties and remarkable sensitivity in the visible to near-infrared region compared to other photodetector samples. The fabricated photodetector confirmed improved quantum performance, especially in the visible spectrum. The work aims to synthesize CuO@ZnO core-shell nanoparticles by a laser ablation technique to improve the electrical properties and spectral response of photodetectors.

https://doi.org/10.53293/jasn.2024.7496.1320, Department of Applied Sciences, University of Technology - Iraq.

1. Introduction

Nanoparticles (NPs) range in size from one to 100 nm in one dimension at least. NPs have gained much attention because of their unique properties, but not much has been documented regarding their risks. Because NP's have

small sizes, large surface areas, and unique chemical and physical properties, they are able to and well-suited to perform numerous different kinds of functions in a variety of applications [1, 2]. The reasons for using oxide metal nanoparticles are owing to their improved qualities. Nanoparticles made of metals and metal oxides have garnered a lot of interest in important substances throughout the last decade, with vast applications across different industries [3]. These substances have been researched extensively across various domains, including in electronics and catalytic processes [4]. Some of the oxide metal nanoparticles, such as ZnO, CuO, MgO, and others, are currently used for numerous processes. Zinc oxide is one such substance with numerous applications due to its high thermal stability and non-toxic nature [3, 5, 6]. On the other hand, copper oxide nanoparticles have found a variety of applications, including the degradation of organic dyes, photovoltaic batteries, and power [7]. It has been discovered over the past few years that surface covering with different semiconductors can greatly enhance the properties of nanoparticles [8, 9]. Researchers have created an entirely novel type of nanoparticles known as hybrid nanoparticles, that are properly organized materials with two, three, or more various kinds of single nanocomponents. Core-shell nanoparticles, also known as core@shell, core-shell, or core/shell nanoparticles, are hybrids. The two nanostructures or more make up core/shell nanoparticles. One nanomaterial serves as the core, while the other is referred to as the shell since it covers the outer layer of the core [10, 11]. Both chemical and physical processes have already been used to create nanoparticles for a variety of substances [12]. Numerous techniques can be used to create nanoparticles, including chemical reactions, sol-gel preparation, thermal breakdown, hydrothermal treatment procedures, and pulsed laser ablation [13].

Combining the characteristics of several oxides of metal and composites to create and further develop new substances with intriguing and attractive characteristics has become increasingly frequent in optoelectronic sensor technologies [14]. The distinctive optical, electrical, and thermal properties of copper oxide (CuO) and zinc oxide (ZnO) render them low-cost, non-toxic semiconductor substances that may be readily synthesized using various methods. The band gaps of these metal oxides may be adjusted during synthesis, enabling customized light absorption across Ultraviolet to Infrared spectral ranges, so rendering them appropriate for photodetector applications. copper oxide is a semiconductor of the p-type characterized by the limited band gap (1.2-2 eV) and significant optical absorption within a visible spectrum [15]. Zinc oxide is an n-type semiconductor characterized by a broad direct band gap of about (3.37 eV), substantial exciton bonding energy (60 meV) at elevated electron mobility (increased to 200 $cm^2 V^{-1} s^{-1}$), and ambient temperature [16]. A kind of II heterojunction is established by combining copper oxide and zinc oxide in the radial core-shell nanoparticle configuration, resulting in a structure appropriate for improved photodetectors with a wide detection range [17]. The asymmetrical gap of a type II heterojunction facilitates the effective separation of charges for photogenerated pairs of electrons and holes across a CuO@ZnO interface, creating an internal electric field, thus improving the absorption of light efficiency [18]. Additionally, CuO@ZnO nanocomposite material thin films may be fabricated using numerous methods, including chemical bath deposition [19], pulsed laser deposition [20], electro-plating [21], spray pyrolysis [22], and diverse sol-gel deposition methods [23], etc. The drop-cast process is the simplest and most economical method for synthesizing thin films [24]. Additionally, the unique optical and electrical properties of these materials are essential for applications in photodetectors and solar energy cells [25, 26]. This study focused on the use of the PLAL method to create core-shell CuO@ZnO colloidal NPs. Different nanoparticle sizes were produced by submerging a Cu and Zn metal target in distilled water. This work is noteworthy because it uses a Nd: YAG laser to modify the electrical properties and spectrum response of a nanoparticle's core-shell solution. A scan electron microscope, X-ray diffraction, UV-visible spectroscope, and transmission electron microscopy were used to examine the nanostructured core-shell materials that were drop-cast onto the porous silicon. This study provides information on how the core-shell structure of CuO@ZnO nanoparticles affects the physical properties and photodetectors' effectiveness of CuO@ZnO colloidal NPs deposited on PSi. The findings of this study have important implications for the development of photodetector and optoelectronic structures that utilize CuO@ZnO NPs core-shell and PSi [24], [25, 26].

2. Material and Experimental part

2.1 Materials

The silicon wafer was obtained from the affiliation of the Tianjin College of Semiconductor Technologies located in Tianjin, China. The silicon wafer exhibits n-type conductivity with a (111) crystallographic

orientation. The silicon wafer underwent polishing on one side, resulting in a diameter of 125±0.3 mm. It has a resistance of 0.001 Ω.cm and a 200 μm thickness. The ethanol and hydrofluoric acid were supplied by Sinopharm Chemical Reagent Co., Ltd., a Spanish supplier. Hydrofluoric acid is the solution of hydrogen fluoride (HF) within water. The HF solution had a 48% concentration and was colorless, acidic, and extremely corrosive. Copper and Zinc materials with 99.99% purity were provided by Sigma Aldrich.

2.2 Preparation of Porous Silicon

The porous silicon (PSi) was created using the photoelectrochemical etching (PECE) method on a single-crystalline silicon (Si) wafer. The initial substance used was the silicon wafer exhibiting crystallographic alignment of (111) and n-type conductivity. A silicon wafer, with a square form and a 2 cm side length, was precisely sliced utilizing a diamond saw. The specimen was cleaned using an ethanol solution and then rinsed for 5 min with distilled water to ensure the total removal of any residual contaminants. Subsequently, the silicon chip was dried, employing a constant stream of dry air. **Fig. 1** illustrates the construction of an electrolytic cell containing a Teflon cell, a Halogen lamp (200 W), a DC power supply (WAIBK.PS-1502), a digital ammeter (TEKTORNICS CDM-250), a rubber O-ring and the two electrodes.

The silicon specimen was inserted inside a rubber substance, such as an O-ring, to allow just the front face of the sample to contact the hydrofluoric acid (HF) solution during the etching procedure. A rubber O-ring was employed to avoid any electrolyte solution leaking. Furthermore, a foil of stainless steel had been connected to the rear of the silicon specimen to ensure optimal electrical connectivity. A photoelectrochemical etching (PECE) technique was performed within an electrolytic cell equipped with two electrodes, wherein a gold electrode served as the cathode and an equipped Si slice served as the anode. Anodization was facilitated by two electrodes in the electrochemical cell, which supplied the current. **Fig. 1** illustrates the construction of an electrolytic cell utilizing Teflon substance to prevent HF from chemical reactions. The electrolytic cell involved a central circular opening measuring 1 cm^2, allowing for interaction directly with the Si wafer.

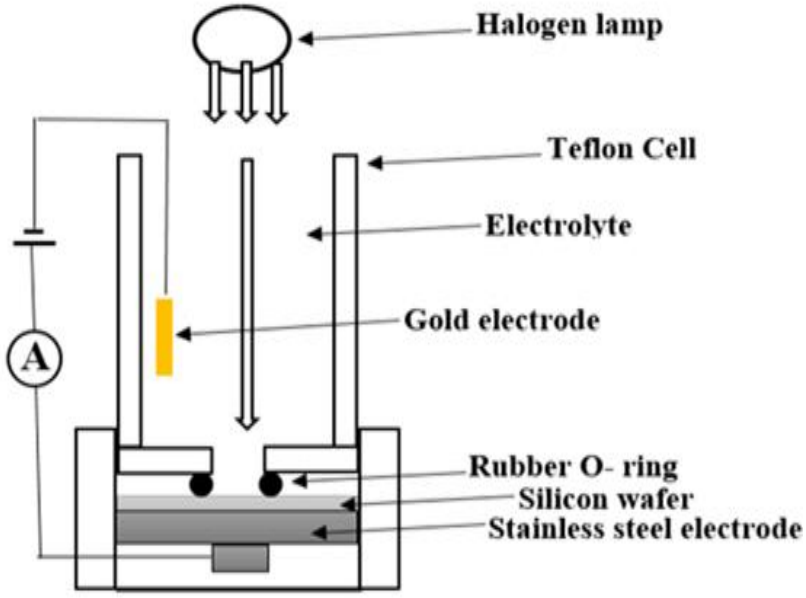

Figure 1: A schematic depiction of photoelectrochemical etching process.

To create PSi samples, the Si pieces were subjected to etching for a duration of 15 min. The etching process was carried out at room temperature with a current density of 15 mA/cm^2 while a 200 W halogen light illuminated the Si piece. The sample was immersed in an HF solution that was reduced to a concentration equal to 24% using ethanol. Ethanol was utilized as a type of surfactant, reducing the frequency bubbles of hydrogen on the top surface of Si. [27]. A specimen was purified by using ethanol and then dehydrated by dry air following the anodization process.

2.3 Laser Ablation Process

The production of zinc oxide nanoparticles (ZnO NPs) and copper oxide nanoparticles (CuO NPs) was carried out by utilizing the laser ablation method. This was accomplished by the process of ablation of a zinc and copper target with a 99.99% high purity level, with 20 mm diameter and 5 mm thickness. The copper and zinc target were immersed within distilled water of about 3 mL and exposed to laser pulsed radiation using a laser Nd: YAG, as shown in **Fig. 2a.** The laser Nd: YAG type Q-switch has a wavelength of 1064 nm, a repetition rate of 1 Hz, and a pulse duration of 10 ns. To obtain the desired laser radiation intensity, the laser pulse energy of 700 mJ at 200 pulses was used. A convex and flat-surfaced lens with a focal length of 110 mm and a spot size of 1.5 mm was used to calculate the intensity when it was pointed at the copper (Cu) and zinc (Zn) metal surfaces. Upon exposure to the surrounding atmosphere, the copper and zinc nanoparticles oxidise and undergo laser ablation to become copper oxide and zinc oxide nanoparticles. The suspension of copper oxide nanoparticles and zinc oxide nanoparticles become transparent. During the ablation process, the color of the liquid changed gradually to a light grey for copper oxide nanoparticles and a dark brown for zinc oxide nanoparticles, as illustrated in **Fig. 2b**.

The CuO@ZnO nanoparticles core-shell was prepared using a two-stage laser ablation procedure. The first stage involves preparing the colloidal solution of CuO NPs via laser ablation utilizing the same steps mentioned above. In the final stage, (99.99%) a high pure Zn target with 20 mm diameter and 5 mm thickness was immersed in a 3 mL solution of CuO NPs, that was produced in the first stage, and then exposed to the ablation process utilizing the same Nd: YAG laser. The parameters govern how the Nd: YAG laser functions. The liquid gradually changed from its original color to a dark brown hue during the ablation process; the CuO/ZnO percentage is 1:1, as depicted in **Fig. 2b**. The absorption spectra were recorded using the Metratech UV-VIS spectrometer following the ablation procedure. The zinc oxide nanoparticle, copper oxide nanoparticle, and CuO@ZnO NPs core-shell colloids solution was analyzed using TEM.

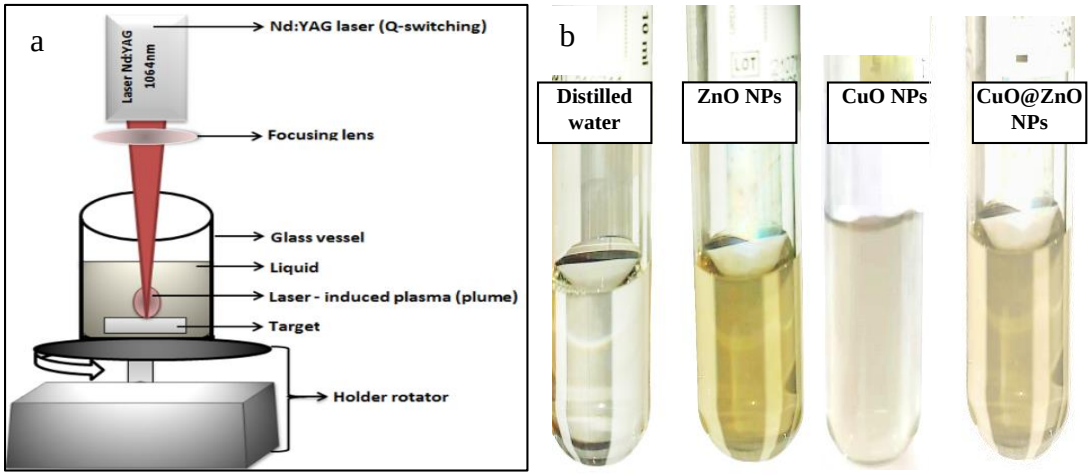

Figure 2: (a) A schematic system of PLAL, (b) Photographs of the color for Zinc oxide, Copper oxide, and CuO@ZnO nanoparticles Core-Shell suspension.

An amount of zinc oxide nanoparticles, copper oxide nanoparticles, and a core-shell structure of CuO@ZnO NPs 30μL were deposited on a PSi surface using a drop-casting approach. This was carried out to investigate the structural and physical characteristics of the zinc oxide nanoparticle, copper oxide nanoparticle, and CuO@ZnO NPs core-shell structure. The process comprises applying 20 droplets of a colloidal solution to the substrate, followed by a 5-minute drying period on a hot plate set at 40 °C. The J-V tests were carried out to evaluate the effectiveness of porous silicon, copper oxide nanoparticles deposit on porous silicon, zinc oxide nanoparticles deposit on porous silicon, and CuO@ZnO nanoparticles core-shell deposit on porous silicon samples. The

measurements were conducted under both light and dark conditions, using power intensities of 25, 65, 110, 150, and 180 mW/cm^2. For the analysis of the electrical properties of the samples, a silver paste was applied to both surfaces of the samples to deposit silver (Ag). The two silver layer connection electrodes had the same area, approximately 0.07 cm^2, and were fabricated using highly pure Ag (99.99%) to ensure ohms connection. The specimens were analyzed utilizing a scanning electron microscope, (Inspect F50) and XRD (SHIMADZU, Japan). Measurements of detectivity (D), quantum efficiency (QE), and responsivity (R_λ) were also performed on each specimen.

3. Results and Discussion

The XRD configuration of porous silicon is shown in **Fig. 3a**. The peak at 2θ angle 28.4° represents the existence of porous silicon that corresponds to the crystallographic plane (111). The peak in porous silicon is becoming boarding with low intensity compared to crystal Si. This is due to the strain effect, which causes a small extended lattice parameter, causing a PSi peak to be shifted to a small diffraction angle. As the crystalline size of PSi decreases, the energy gap increases. **Fig. 3b** depicts the XRD configuration of copper oxide nanoparticles embedded in porous silicon. The CuO nanoparticles were produced utilizing laser energy of about 700 mJ. The primary peaks of CuO nanoparticles have been identified at angles of 32.12°, 46.2°, 51.28°, and 58.48°. The peak values of diffraction are caused by the reflection for layers along distinct crystallographic planes, specifically (110), (002), (112), and (202). These peaks indicate a unique polycrystalline composition of CuO NPs. The peak diffraction patterns of CuO NPs exhibited a strong similarity to the monoclinic structure indicated by JCPDS card No. 45-0937 [28]. A Scherrer equation is utilized to determine the crystallites' particle size, as shown in **Table 1**. The average size measurements of CuO NPs/PSi sample's crystallites all fall within the nanometric range of 10.73 to 32.04 nm.

Fig. 3c depicts the XRD configuration of zinc oxide nanoparticles embedded in porous silicon. The ZnO NPs were produced by utilizing a 700 mJ energy laser pulse. The primary peaks at 2θ angles 34.8°, 36.4°, 47.6°, 56.6°, and 63.2° indicates existence zinc oxide nanoparticles. Peaks of diffraction results from the reflection of layers along certain crystalline planes that have Miller indices, specifically (002), (101), (102), (110), and (103). The specific peaks reveal a unique polycrystalline composition of zinc oxide nanoparticles. The peak patterns of diffraction ZnO NPs exhibited a strong similarity with the hexagonal wurtzite arrangement, as indicated by JCPDS card No. 36-1451) [29]. Scherrer's equation was employed to determine the nanoparticle volume of the crystallites, as displayed in **Table 2**. The average volume measurements for the ZnO NPs/PSi sample's crystallites all fall within the nanometer range of 29.78 to 59.79 nm [26, 27].

The XRD analysis of the nanoparticle's core-shell deposited on a PSi substrate is depicted in **Fig. 3d**. The core-shell of CuO@ZnO NPs was synthesized utilizing a 700 mJ laser pulse energy, a 1064 nm wavelength, and a series of 200 repeated pulses. The XRD investigation confirmed the nanoparticle's core-shell and its crystal structure. The task included comparing the diffraction angles (2Θ) of CuO and ZnO using the details specified in a JCPDS card No. provided in the existing literature. A pattern of XRD was acquired by quantifying the angles of scattering (2Θ^o) throughout a range of 30^o to 70^o to the core-shell nanoparticles. The XRD examination of the nanoparticle core-shell displayed peaks at 31.48 ^{o} and 56.56^o that corresponded to a ZnO crystalline structure. The peaks were explicitly identified as the Miller indices (100) and (110), respectively. The ZnO specimen displayed the hexagonal wurtzite structure, which was verified with JCPDS No. 36-1451 [4]. Moreover, it was ascertained that peaks found at 36.72^o and 62.6^o diffraction angles correspond to the planes (111) and (-113) of crystal for CuO, respectively. The diffraction peaks of CuO demonstrate a remarkable alignment that matches the monoclinic structure of a crystal, which was verified with JCPDS card number 45-0937 [4]. An optimum threshold for copper (Cu) was established at 43.76^o. The peaks of diffraction are indicative of surfaces that reflect light along specific planes. A conventional polycrystalline Cu structure is denoted by the (111) orientation. Scherrer's equation was employed to determine the nanoparticle volume of the crystallites, as displayed in **Table 3** [24, 26, 30].

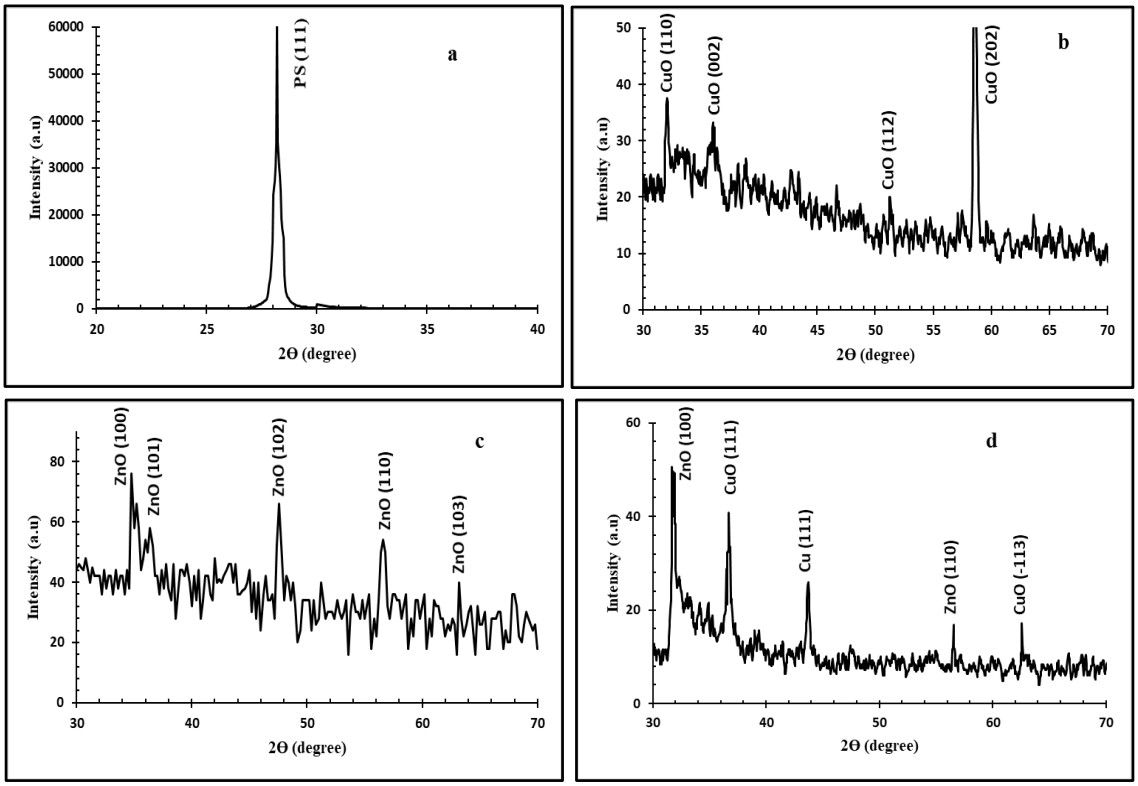

Figure 3: The XRD schemes of (a) Porous Silicon, (b) Zinc Oxide NPs/PSi, (c) Copper Oxide NPs/PSi and (d) CuO@ZnO NPs/PSi.

Table 1: The Size of crystallites for Copper Oxide nanoparticles deposited on porous silicon.

Position of peak (2Θ)	Miller indices	Crystals size (nm)	FWHM (in rad.)
32.12	(110)	32.04	0.004502949
36.16	(002)	10.73	0.013596115
51.28	(112)	30.18	0.005096361
58.48	(202)	23.22	0.006841691

Table 2: The size of crystallites for Zinc Oxide nanoparticles deposited on porous silicon

Position of peak (2Θ)	Miller indices	Crystals size (nm)	FWHM (in rad.)
34.8	(002)	43.13	0.003368485
36.4	(101)	39.63	0.003682645
47.6	(102)	35.15	0.004310963
56.6	(110)	29.78	0.005288348
63.2	(103)	59.79	0.002722714

Table 3: The size of crystallites for core shell nanoparticles deposited on porous silicon.

Sample	Position of peak (2Θ)	Miller indices	Crystals size (nm)	FWHM (in rad.)
ZnO	31.48	(100)	23.65	0.006091199
CuO	36.72	(111)	23.85	0.006126106
ZnO	56.56	(110)	35.8	0.00439823
CuO	62.6	(-113)	95.85	0.001692969
Cu	43.76	(111)	22.06	0.006771877

Scanning electron microscopy images of porous silicon, copper oxide, zinc oxide, and CuO@ZnO core-shell nanoparticles are displayed in **Fig. 4**. All nanoparticles were prepared using a 700mJ laser ablation energy at 200 pulses and 1064 nm of laser wavelength and deposited onto porous silicon specimens. The surface images and results demonstrate that the porous silicon layers have a porous structure like that of the sponge. **Fig. 4a** illustrates the semi-circular shape of the pores. That has to do with the quick degradation of silicon's outer layer brought on by exposure to a solution of hydrofluoric acid, which rapidly erodes the surface and is followed by oxidation [9]. **Fig. 4b, c**, and **d** show CuO, ZnO, and CuO@ZnO nanoparticles, respectively, represented as luminous grey dots of different sizes that resemble spherical grains. Both on the surface and inside the porous silicon, the nanoparticles are dispersed randomly [24, 25, 27].

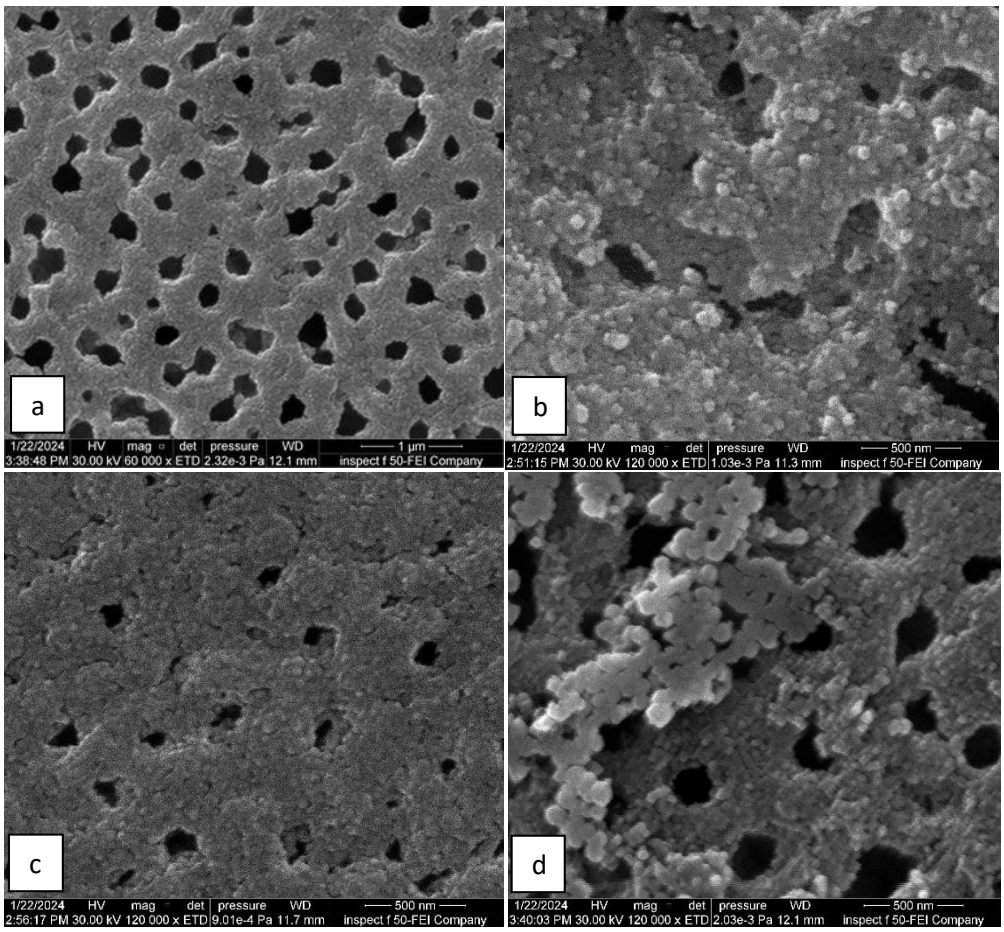

Figure 4: SEM photos of (a) PSi, (b) Copper Oxide nanoparticles/PSi, (c) Zinc Oxide nanoparticles /PSi, and (d) CuO@ZnO NPs/PSi Core-Shell.

Fig. 5 exhibits transmission electron microscope (TEM) images of copper oxide, zinc oxide, and CuO@ZnO nanoparticles core-shell colloidal solutions. Copper oxide, zinc oxide, and CuO@ZnO colloidal nanoparticles core-shell were synthesized with laser energy at 700 mJ for 200 pulses and wavelength 1064 nm**. Fig. 5a** exhibits TEM pictures of CuO NPs and size distribution. The size determined from TEM analysis results closely matches the size calculated using the Scherrer equation derived from the X-ray diffraction (XRD) results. After careful examination, the copper oxide nanoparticles produced by laser ablation have a spherical form and a strong tendency to aggregate, forming patterns resembling chains. The original substance's metallic oxide properties and the process of nanoparticle formation are to blame for this [31].

TEM image of ZnO NPs and their shape distribution are shown in **Fig. 5b**. The image shows that the structure of the synthesised nanoparticles is irregularly shaped, with some of them matching the hexagonal form of wurtzite. This confirms that the results were derived from X-ray diffraction and that the average sizes of the particles are on the nanometre scale. **Fig. 5c** shows the TEM image of the CuO@ZnO NPs core-shell which were produced

by a laser ablation process with 700mJ for 200 pulses. This picture also shows how the different morphologies of the nanoparticles are distributed. It shows that the core-shell of the generated nanoparticle has a spherical shape with some irregularities. The nanocomposite exhibits a core-shell structure, with a slightly lighter exterior component made of a ZnO nano-shell and a dark central region made up of CuO nanoparticles [24].

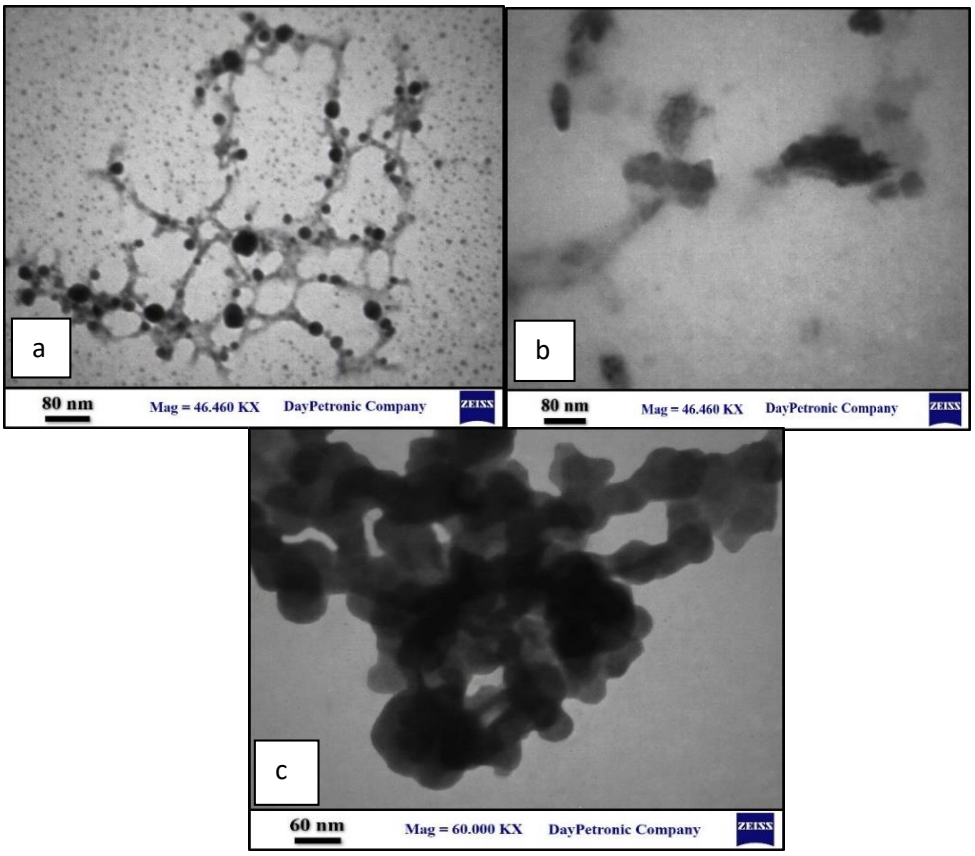

Figure 5: The TEM photos of (a) Copper Oxide nanoparticles, (b) Zinc Oxide nanoparticles, and (c) CuO@ZnO NPs Core-Shell.

CuO@ZnO core-shell structures have higher absorption intensity in the Ultraviolet and visible regions compared to pure CuO and ZnO. The measured absorbance in pure ZnO and CuO is due to electronic transitions that take place valence band from the orbitals (2p) of oxygen ion (O^{2-}) to the conduction band of metal ion's orbitals (3d/4s). The absorption in these locations is intensified due to the low transitions of energy for oxygen ion O^{2-} (2p) → Zn^{2+} (3d/4s) in comparison to O^{2-} (2p) → Cu^{2+} (3d). Applying ZnO to the surface of CuO results in the formation of two closely situated conduction bands. This phenomenon occurs due to the existence of shared surface oxide molecules between the Zn^{2+} and Cu^{2+} surface levels. Moreover, it is significant to acknowledge the importance of d-d transitions in enhancing the absorption from the closely situated Zn^{2+} and Cu^{2+} levels. Consequently, as the thickness of the shell grows, the degree of absorption also rises [32].

Fig. 6a exhibits the absorption spectra of zinc oxide nanoparticles, copper oxide nanoparticles, and CuO@ZnO core-shell nanoparticles in a suspension that was synthesized with 700 mJ for 200 shots at 1064nm of the laser wavelength. The generated CuO NPs, ZnO NPs, and CuO@ZnO colloidal NPs showed absorbance at wavelengths between 250 and 360 nm, 220 and 380 nm, and 200 and 400 nm, respectively, in their UV absorption spectra. Within the wavelength range, the CuO@ZnO colloidal solution's nanoparticle core-shell exhibits an absorption peak between 300 and 400 nm [4]. The nanoparticles core-shell of CuO@ZnO, nanoparticles of zinc oxide, and nanoparticles of copper oxide, which include wide peaks observed in the spectra demonstrate the characteristics of colloidal solutions and contain nanoparticles of different shapes and sizes. This conclusion is supported by the results of scan electron microscope (SEM) and transmission electron microscope (TEM) investigations. The CuO@ZnO NPs core-shell heterojunction significantly improves the

absorption of visible light compared to the pure ZnO, resulting in increased utilization of light and generation of additional charge carriers through photoexcitation [33]. **Fig. 6b, c,** and **6d** show the relationship between the square of $(\alpha hv)^2$ and (hv) for copper oxide nanoparticles, zinc oxide nanoparticles, and CuO@ZnO nanoparticles core-shell, respectively. The least amount of energy required to move an electron from the valence band to the conduction band is known as the energy gap (Eg). **Table 4** shows that the Eg of ZnO NPs, CuO NPs, and CuO@ZnO NPs colloidal solutions differ by 3.2, 3.4, and 2.8 eV, respectively.

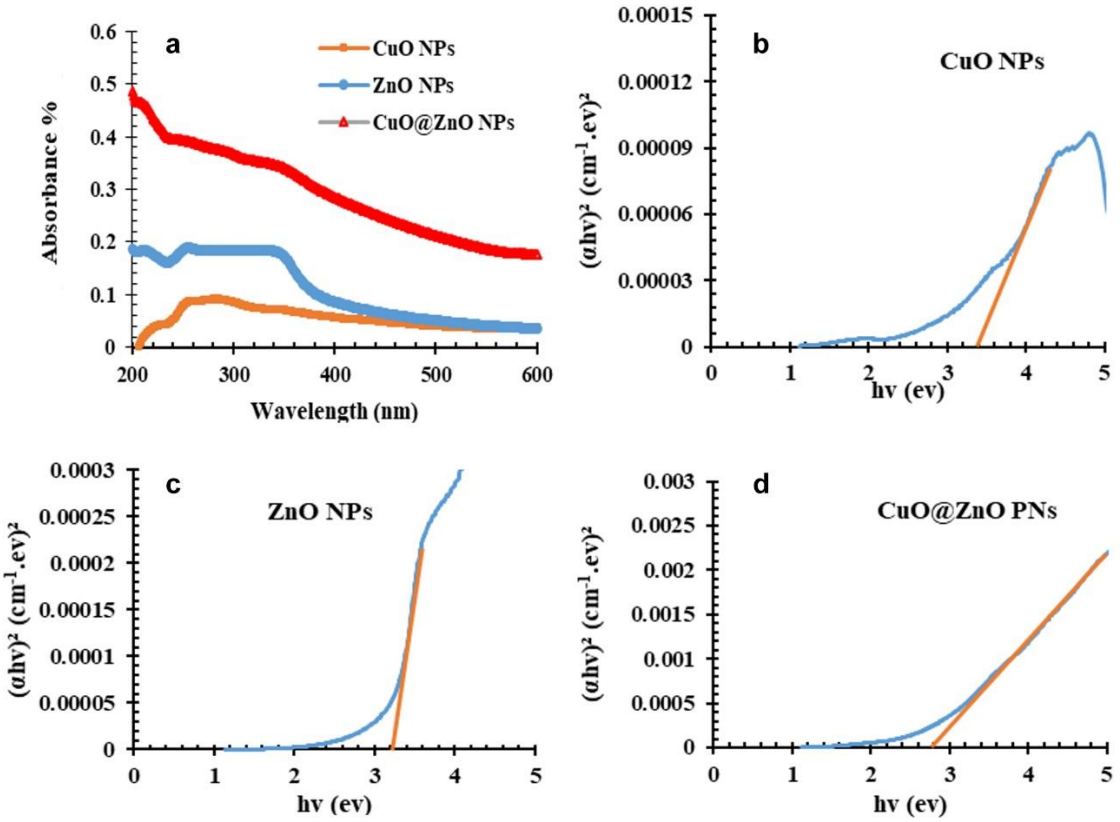

Figure 6: (a) Ultraviolet-visible spectra graph, (b) (αhv)2 plotted with the energy of the photon for Copper Oxide NPs, (c) Zinc Oxide NPs, and (d) CuO@ZnO NPs Core-Shell.

Table 4: Shapes and dimensions of the samples according to the standard specification.

Samples	Pulses number	Laser pulses energy	Absorption peak (nm)	Energy gap (eV)
CuO NPs	200 shots	700	220-380	3.4
ZnO NPs			250-360	3.2
CuO@ZnO NPs			200- 400	2.8

Due to some interrelated factors, the band gap energy decreases when the size of the CuO@ZnO particles decreases. Quantum confinement has a significant impact; as particle size decreases, spatial confinement for charge carriers (holes and electrons) increases, which typically results in a band gap expansion. This effect can be lessened in the CuO@ZnO case by adding imperfections and interface states, which are more noticeable in particles with smaller sizes. Because of the increased surface area and defect states, the combination of copper oxide and zinc oxide results in a decrease within a band gap. CuO@ZnO nanocomposites demonstrate how the interaction between CuO and ZnO nanoparticles affects a band gap because of interfacial interactions [24, 27, 31].

Fig. 7 shows the current-voltage (J-V) curves for four sandwich samples that generated by providing DC voltages in both reverse and forward bias modes with a voltage ranging from -5 to 5 V. In the first sandwich sample, a silver electrode is deposited on top of a porous silicon layer that is above negative silicon. In the same manner as the first sandwich sample, the other sandwich samples are included. They differ only by adding a layer of thin film of nanoparticles between the silver electrode and porous silicon. The second sample includes a thin film layer of CuO NPs. The third sandwich sample presents a thin film layer from ZnO NPs. The fourth sandwich sample includes a thin film layer from CuO@ZnO NPs core-shell. The J-V curves of all samples exhibited rectifying exhibited rectifying properties and displayed distinct properties like Schottky diode, caused by the formation of hetero-junction nanostructures occurring between the (copper oxide NPs, zinc oxide NPs, and CuO@ZnO NPs) with porous silicon layer and between porous silicon layer and silicon substrates [34]. There is a significant disparity in energy levels between CuO, ZnO, and CuO@ZnO with PS, leading to the creation of the heterojunction nanostructure. The current exhibits an exponential increase with voltage, as shown by the current-voltage curve measurements for the sandwich samples under the forward bias condition. However, at reverse bias, the leakage current in the dark significantly decreases, enabling the samples to be used as effective current rectifiers. The increase in the current density with a voltage bias under the forward applied may be explained by the reduction in the depletion region with width across the junctions. On the other hand, a reverse bias causes the depletion region to thicken, which lowers current because there is less electric charge moving through it [25, 26, 27].

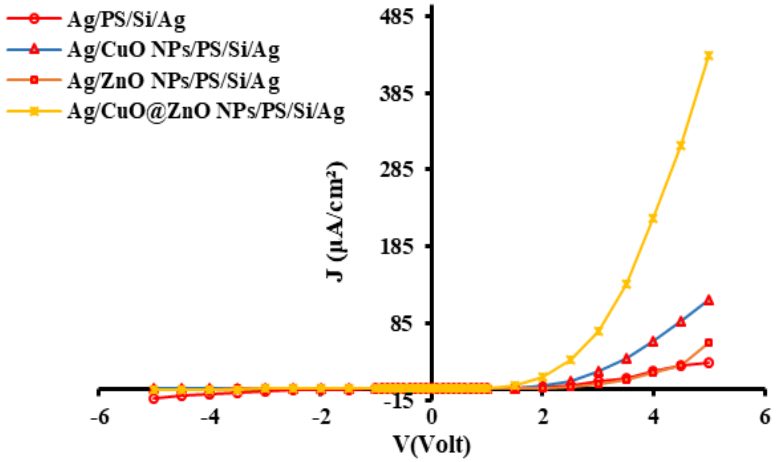

Figure 7: J-V characteristics of the sandwich PSi specimen and sandwich PSi samples based on thin films colloidal NPs CuO@ZnO NPs, CuO NPs, and ZnO NPs.

The current density passing through the sandwich specimens synthesized from zinc oxide nanoparticles, copper oxide nanoparticles, and CuO@ZnO core-shell nanoparticles increased under forward bias compared to the sandwich specimen synthesized from PSi. The specimen's porous silicon layer exhibited significant porosity due to its large pore diameters, causing a substantial disturbance to the structure of porous silicon. Consequently, the movement of electrons was hindered on the photosensitive side of porous silicon of the silicon structure. The influence of quantum particle confinement may be responsible for the energy difference between the valence and conduction bands in PSi. The carrier's charged number within the material decreases as a result of the quantum confinement. [35].

The current-voltage characteristics curves demonstrated a significant current density flow via the sandwich specimens synthesized from CuO@ZnO NPs. The potential cause for the observed increase in current density might be a modification in the nanoparticle size of CuO@ZnO NPs, resulting in a decrease in resistivity and energy gap compared to zinc oxide nanoparticle and copper oxide nanoparticle individually. The outcome aligns with the Uv-Vib test, as the CuO@ZnO NPs specimen exhibited a reduced energy gap of 2.8 eV.

The basic idea of a photodetector is that incident radiation or light that falls on the surface of a detector and is absorbed is converted into electrical signals. A photodetector works like a p-n junction that is biased in the

opposite direction. The operation of a photodetector involves three processes: Absorption, carrier extraction as photocurrent and carrier transport. During the absorption process, light energy falls on the photodetector and is absorbed by the atoms of the photodetector. The light emits small packets of energy called photons, resulting in the absorption of multiple photons by the photodetector atoms. Consequently, the device generates charged charge carriers. Electron-hole pairs form the charge carriers, which are mobile charge carriers. During this process, the generated carriers are moved through each absorption zone. Certain photodetectors provide gain to charge carriers, which causes the photon multiplication to increase during carrier extraction and transmission, similar to a photocurrent. After electric charges (electron-hole couples) successfully pass through the circuit outside as an electrical signal, these charge carriers are collected. Photocurrent is the term used to describe a current that is primarily generated by photons incident on a photodetector. Metal-semiconductor Metallic photodiodes are alternatively referred to as Schottky-barrier photodiodes. The photodiodes are constructed using metal-semiconductor heterojunctions. The CuO nanoparticles, ZnO nanoparticles, and CuO@ZnO nanoparticles are classified as metals, while PSi is categorized as a semiconductor. The thin semi-transparent metallic film substitutes for the n-type or p-type layer within a p-n junction of a photodiode. A thin film primarily consists of a hybrid metal-semiconductor mixture that functions as a metal. The Schottky barrier photodiode exhibits rapid response times and extensive operational bandwidth.

Fig. 8 depicts the photocurrent characteristics of the sandwich specimens synthesized from PSi, CuO@ZnO NPs, CuO NPs, and ZnO NPs in the existence of white light under the influence of an inverse bias voltage. The investigation was performed at room temperature, applying different power values (25, 65, 110, 150, and 180 mW/cm^2). When a volt is applied in reverse bias, the photocurrent is only observed, and the reverse current is considerably enhanced by light irradiation. As a result, there is a substantial increase in the inner electric field intensity, the likelihood of separation of electrons from the hole, and the formation of a depletion area. More precisely, the light that penetrates within the depletion region initiates the creation of hole-electron pairs. A photocurrent shows an increase with increasing intensity of the incident light and an inverse bias voltage, as this intensifies the separation between electrons and holes.

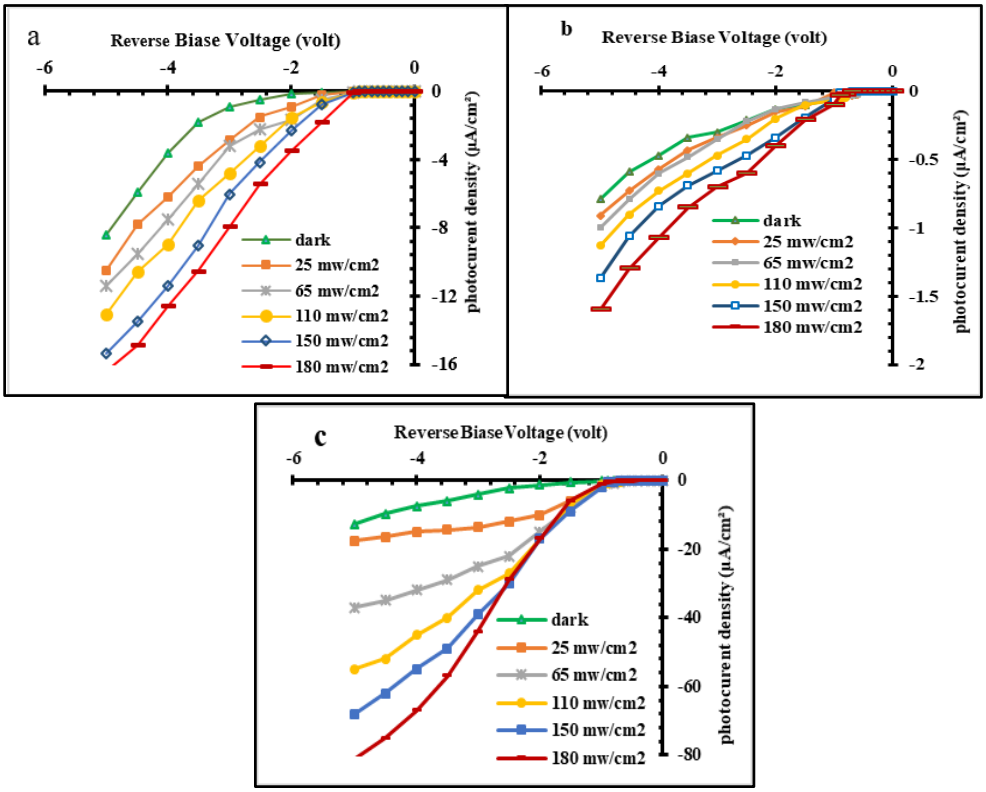

Figure 8: Photocurrent J–V characteristics of the sandwich specimens synthesized from (a) Copper Oxide NPs, (b) Zinc Oxide NPs, and (c) CuO@ZnO NPs.

The CuO@ZnO heterojunction exhibits a substantial enhancement in the absorption of visible light when compared to pure CuO and ZnO, which is advantageous for harvesting light and generating larger photo-generated charge carriers [33]. As a result, there are more electrons and holes, demonstrating the sandwich sample's capacity to function as a photodetector. When the sandwich specimen was made with CuO@ZnO NPs core-shell, the photocurrent measurement showed an increase. Numerous factors, including the enhancement of the core-shell connection between CuO@ZnO nanoparticles and porous silicon, the expansion of the depletion region, the reduction of the trap state density, and the extension of a carrier's diffusion length, can be attributed to the outcomes [25, 27].

As shown in **Fig. 8a, b**, and **c**, the photocurrent density of the copper oxide nanoparticle sample was about 16 mA/cm2, about 0.5 μA/cm2 for the zinc oxide nanoparticle sample, and about 80 μA/cm2 for the CuO@ZnO NPs sample. When the electrons hit CuO, they move from the Fermi level (Ef) of ZnO to CuO, which improves the photocurrent in the CuO@ZnO NPs core-shell sample. When their Ef levels eventually equalize, band bending occurs at the interface. When the reverse potential increases, the bands are also bent, and the charge transfer is favored. Consequently, the photocurrent increases [37].

The findings show that, following the addition of thin films made of CuO@ZnO NPs core shell, CuO NPs, and ZnO NPs, as shown in **Fig. 9a,** the photodetectors exhibit exceptional sensitivity to a wide range of wavelengths, from the visible to almost infrared. The CuO and CuO@ZnO layer exhibits higher responsivity to visible light regions compared to lower responsivity to visible and infrared light regions, attributed to the present of porous silicon and silicon, respectively. **Fig. 9a** illustrates three distinct regions of spectra responsivity within the photodetector specimens. The primary spectral range, centered at 450 nm of a wavelength, represents the point at which the CuO and CuO@ZnO layer absorbs light while the ZnO at 400nm. The second spectra region, located at 700 nm of a wavelength, is associated with the absorbance of the PSi layer [36, 37]. Silicon in the manufactured sandwich samples was responsible for detecting the third spectra range at 900 nm of a wavelength.

When the core shell of CuO@ZnO nanoparticles was present, the photodetector sample showed increased spectrum responsiveness. The photodetector specimen made with zinc oxide nanoparticles had a 0.05 A/W spectral responsivity at 450 nm wavelength. However, a photodetector sample made with CuO@ZnO nanoparticles core-shell showed an improvement in spectral responsivity between 0.05 and 0.2 A/W, specifically at a wavelength of 355 nm. Changing the type of thin film deposited resulted in a change in the shape of the spectral responsivity towards longer wavelengths. Variations in the thin-film energy gap for CuO@ZnO nanoparticles, copper oxide nanoparticles, and zinc oxide nanoparticles may be the cause of this behaviour. The spectral response (R_λ) of the copper oxide nanoparticle-based photodetector device is approximately 0.1 A/W. The increased diffusion length and the expansion of a depletion region, the decrease in the density of surface states, the increased efficiency of charge carriers, the expansion of a light absorption area, the reduction of dark current, and the enhanced light absorption are some of the factors that contribute to a photodetector's improved responsivity (Rλ). The photodetector created with a CuO@ZnO NPs thin film achieved a maximum detectivity (D) of around 64.9×10^{10} Jones (cm. $Hz^{1/2}$/W) at 700 nm of a wavelength. **Fig. 9b** demonstrates how the type of thin film affects the detectivity of photodetectors. The spectral responsivity and the spectral detectivity curves exhibit similar patterns. The detectivity increased from around 10×10^{10} to 44×10^{10} Jones at a wavelength of 450 nm after the thin film type changed from PSi to CuO@ZnO NPs. It can be inferred that the photodetector exhibited a minimal level of noise in its substantial level of responsivity or a dark current. The improved performance of the photodetector can be attributed to the reduction in trapping sites, current leakage, structural flaws, and surface imperfections. The photodetectors examination was performed on the photodetectors sandwich specimens synthesized from PSi, CuO@ZnO nanoparticles core-shell, copper oxide nanoparticles, and zinc oxide nanoparticles to calculate their Q.E. The results showed that Q.E values of 20.3%, 13.5%, and 37.83% at a 700 nm wavelength, as shown in **Fig. 9c** [37].

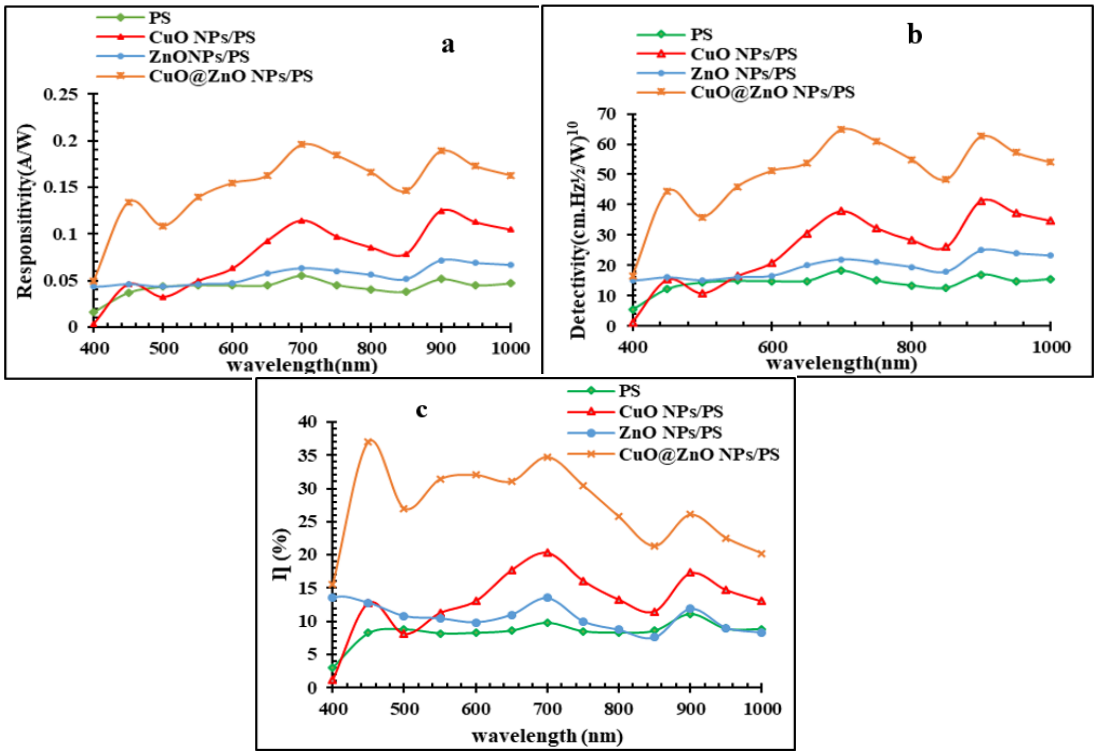

Figure 9: The spectra of (a) R_λ, (b) D, and (c) Q.E for PSi, CuO NPs/PSi, ZnO NPs/PSi, and CuO@ZnO NPs /PSi samples.

4. Conclusion

The main goal of this study is to produce colloidal solutions of ZnO NPs, CuO NPs, and core-shell CuO@ZnO NPs. The laser ablation process creates a colloidal solution that is embedded in porous silicon substrates by the drop-casting method as thin films. The study investigates the influence of the ZnO NPs and CuO NPs samples when converted into core-shell, on the structural characteristics, and electrical, morphological, and optical properties, specifically for their use in photodetector applications. The XRD examination showed a distinct peak pattern of diffraction at various angles, demonstrating the existence of PSi, ZnO, CuO, and CuO@ZnO materials. The SEM image illustrates that the CuO, ZnO, and core-shell nanoparticles showed randomly distributed spherical nanoparticles, whereas the structure of PSi is porous and sponge-like. A TEM picture demonstrated a core-shell structure, with a dark central region consisting of CuO nanoparticles and a somewhat lighter outside component composed of a ZnO nanoshell. The images of TEM also revealed the size and shape of the nanoparticles, which vary depending on the type of sample.

The optical properties of the produced samples were examined by utilizing UV–vis absorbance spectroscope. The CuO@ZnO core-shell nanoparticles showed the lowest energy gap around 2.8 eV. The J-V characteristics of the samples were analyzed both with and without illumination. A notable improvement was observed in the synthesis of photodetectors using core-shell nanoparticles. The photodetectors showed exceptional responsivity and rectifying capabilities across a wide range of wavelengths, from visible light to near-infrared. Furthermore, the produced photodetectors showed enhanced Q.E., especially in the visible range. The study's conclusions have significant ramifications for the development of photodetector and optoelectronic systems that make use of porous silicon and CuO@ZnO NPs core-shell.

Authors' contributions

Author contributions **Salah M. Abdul Aziz** -Writing Original draft, Methodology, Investigation, and Formal analysis. **Uday M. Nayef, Mohammed Rasheed** -Main Concept, Data interpretation, and supervision. **Uday M. Nayef** -Writing-Review and editing, Visualization, and Data curation.

Funding
No funded

Acknowledgments
The authors would like to thank the University of Technology-Iraq for the logistic support this work.

Conflicts of Interest
The authors declare have no conflict of interest.

References

[1] N. K. Kaushik *et al.*, "Plasma and nanomaterials: Fabrication and biomedical applications," *Nanomaterials*, vol. 9, no. 1, p. 98, 2019.
[2] K. Zhou, X. Zhou, J. Liu, and Z. Huang, "Application of magnetic nanoparticles in petroleum industry: A review," *J. Pet. Sci. Eng.*, vol. 188, p. 106943, 2020.
[3] P. Mahajan, A. Singh, R. Datt, V. Gupta, and S. Arya, "Realization of inverted organic solar cells by using sol-gel synthesized ZnO/Y 2 O 3 core/shell nanoparticles as electron transport layer," *IEEE J. Photovolt.*, vol. 10, no. 6, pp. 1744–1749, 2020.
[4] R. S. Mohammed, K. A. Aadim, and K. A. Ahmed, "Synthesis of CuO/ZnO and MgO/ZnO core/shell nanoparticles with plasma jets and study of their structural and optical properties," *Karbala Int. J. Mod. Sci.*, vol. 8, no. 2, pp. 88–97, 2022.
[5] S. Arya *et al.*, "influence of processing parameters to control morphology and optical properties of Sol-Gel synthesized ZnO nanoparticles," *ECS J. Solid State Sci. Technol.*, vol. 10, no. 2, p. 023002, 2021.
[6] A. Indriyani, Y. Yulizar, R. T. Yunarti, D. O. B. Apriandanu, and R. M. Surya, "One-pot green fabrication of BiFeO3 nanoparticles via Abelmoschus esculentus L. leaves extracts for photocatalytic dye degradation," *Appl. Surf. Sci.*, vol. 563, p. 150113, 2021.
[7] D. O. B. Apriandanu and Y. Yulizar, "Tinospora crispa leaves extract for the simple preparation method of CuO nanoparticles and its characterization," *Nano-Struct. Nano-Objects*, vol. 20, p. 100401, 2019.
[8] A. J. Hadi, U. M. Nayef, F. A.-H. Mutlak, and M. S. Jabir, "High-Efficiency Photodetectors Based on Zinc Oxide Nanostructures on Porous Silicon Grown by Pulsed Laser Deposition," *Plasmonics*, vol. 19, no. 2, pp. 577–593, 2024.
[9] H. T. Hussein, M. K. A. Mohammed, R. I. Kamel, and U. M. Nayef, "Improved sensing performance of porous silicon photodetector with CuO nanoparticles," *Chem. Pap.*, vol. 75, no. 12, pp. 6257–6264. 2021.
[10] M. B. Gawande *et al.*, "Core–shell nanoparticles: synthesis and applications in catalysis and electrocatalysis," *Chem. Soc. Rev.*, vol. 44, no. 21, pp. 7540–7590, 2015.
[11] M. Khatami, H. Q. Alijani, and I. Sharifi, "Biosynthesis of bimetallic and core–shell nanoparticles: their biomedical applications – a review," *IET Nanobiotechnol.*, vol. 12, no. 7, pp. 879–887, Oct. 2018.
[12] Y. R. Parauha, V. Sahu, and S. J. Dhoble, "Prospective of combustion method for preparation of nanomaterials: A challenge," *Mater. Sci. Eng. B*, vol. 267, p. 115054, 2021.
[13] R. Sagheer, S. T. Khadija, Z. N. Kayani, and S. Riaz, "Structural, optical and magnetic properties of ZnO nanoparticles tailored by 'La3+'ions," *Optik*, vol. 244, p. 166816, 2021.
[14] I. S. Brandt, M. A. Tumelero, S. Pelegrini, G. Zangari, and A. A. Pasa, "Electrodeposition of Cu2O: growth, properties, and applications," *J. Solid State Electrochem.*, vol. 21, no. 7, pp. 1999–2020, Jul. 2017.
[15] M. A. Cruz, D. Sanchez-Martinez, and L. M. Torres-Martínez, "CuO thin films deposited by DC sputtering and their photocatalytic performance under simulated sunlight," *Mater. Res. Bull.*, vol. 122, p. 110678, 2020.
[16] C. Florica, A. Costas, A. Kuncser, N. Preda, and I. Enculescu, "High performance FETs based on ZnO nanowires synthesized by low cost methods," *Nanotechnology*, vol. 27, no. 47, p. 475303, 2016.
[17] A. Costas, C. Florica, N. Preda, A. Kuncser, and I. Enculescu, "Photodetecting properties of single CuO–ZnO core–shell nanowires with p–n radial heterojunction," *Sci. Rep.*, vol. 10, no. 1, p. 18690, 2020.
[18] Z. Zheng, X. Zu, Y. Zhang, and W. Zhou, "Rational design of type-II nano-heterojunctions for nanoscale optoelectronics," *Mater. Today Phys.*, vol. 15, p. 100262, 2020.
[19] H. A. Jasim, O. A. A. Dakhil, and A. Maleki, "Synthesis of CuO Nanrods Using Chemical Bath Deposition for a Nonenzymatic Glucose Biosensor," *Al-Mustansiriyah J. Sci.*, vol. 34, no. 1, pp. 97–103, 2023.

[20] A. Al Baroot, M. Alheshibri, Q. A. Drmosh, S. Akhtar, E. Kotb, and K. A. Elsayed, "A novel approach for fabrication ZnO/CuO nanocomposite via laser ablation in liquid and its antibacterial activity," *Arab. J. Chem.*, vol. 15, no. 2, p. 103606, 2022.

[21] I. Shaheen *et al.*, "Electrophoretic fabrication of ZnO/CuO and ZnO/CuO/rGO heterostructures-based thin films as environmental benign flexible electrode for supercapacitor," *Chemosphere*, vol. 322, p. 138149, 2023.

[22] D. Saravanakkumar *et al.*, "Synthesis and characterization of ZnO–CuO nanocomposites powder by modified perfume spray pyrolysis method and its antimicrobial investigation," *J. Semicond.*, vol. 39, no. 3, p. 033001, 2018.

[23] A. M. M. Musa, M. Rasadujjaman, M. A. Gafur, and A. T. M. K. Jamil, "Synthesis and characterization of dip-coated ZnO–CuO composite thin film for room-temperature CO_2 gas sensing," *Thin Solid Films*, vol. 773, p. 139838, 2023.

[24] S. M. A. Aziz, U. M. Nayef, and M. Rasheed, "Synthesis of CuO@ZnO Nanoparticle Core–Shell Formed via Laser Ablation in Liquid for Photocatalytic Applications," *Plasmonics*, Aug. 2024.

[25] S. M. A. Aziz, U. M. Nayef, and M. Rasheed, "Synthesis of Copper Oxide Nanoparticles via Laser Ablation in Liquid for Enhancing Spectral Responsivity," *Plasmonics*, Aug. 2024.

[26] A. Costas, C. Florica, N. Preda, C. Besleaga, A. Kuncser, and I. Enculescu, "Self-connected CuO–ZnO radial core–shell heterojunction nanowire arrays grown on interdigitated electrodes for visible-light photodetectors," *Sci. Rep.*, vol. 12, no. 1, p. 6834, 2022.

[27] S. M. A. Aziz, U. M. Nayef, and M. Rasheed, "Enhancing Spectral Responsivity of Zinc Oxide Nanoparticles via Laser Ablation on Porous Silicon," *Plasmonics*, Jul. 2024.

[28] V. Gopinath *et al.*, "In vitro toxicity, apoptosis and antimicrobial effects of phyto-mediated copper oxide nanoparticles," *RSC Adv.*, vol. 6, no. 112, pp. 110986–110995, 2016.

[29] S. S. Khudiar, F. A.-H. Mutlak, and U. M. Nayef, "Synthesis of ZnO nanostructures by hydrothermal method deposited on porous silicon for photo-conversion application," *Optik*, vol. 247, p. 167903, 2021.

[30] J. Montero *et al.*, "Copper–zinc oxide heterojunction catalysts exhibiting enhanced photocatalytic activity prepared by a hybrid deposition method," *RSC Adv.*, vol. 11, no. 17, pp. 10224–10234, 2021.

[31] S. M. A. Aziz, U. M. Nayef, and M. Rasheed, "Prepared copper oxide nanoparticle colloidal solution by different laser ablation energy in liquid for enhanced organic dye degradation efficiency," *J. Opt.*, Sep. 2024.

[32] S. S. Kumar, P. Venkateswarlu, V. R. Rao, and G. N. Rao, "Synthesis, characterization and optical properties of zinc oxide nanoparticles," *Int. Nano Lett.*, vol. 3, no. 1, p. 30, Dec. 2013, doi: 10.1186/2228-5326-3-30.

[33] L. Zhu, H. Li, Z. Liu, P. Xia, Y. Xie, and D. Xiong, "Synthesis of the 0D/3D CuO/ZnO Heterojunction with Enhanced Photocatalytic Activity," *J. Phys. Chem. C*, vol. 122, no. 17, pp. 9531–9539, May 2018.

[34] A. Ramizy, "Formation and photoluminescence properties OF porous silicon/copper oxide nanocomposites fabricated via electrochemical deposition technique for photodetector application," 2021, Accessed: Jul. 31, 2024.

[35] U. M. Nayef, M. W. Muayad, and H. A. Khalaf, "ZnO/PS/p-Si heterojunction properties," *Eur. Phys. J.-Appl. Phys.*, vol. 66, no. 2, p. 20104, 2014.

[36] N. A. Abdulkhaleq, A. K. Hasan, and U. M. Nayef, "Enhancement of photodetectors devices for silicon nanostructure from study effect of etching time by photoelectrochemical etching Technique," *Optik*, vol. 206, p. 164325, 2020.

[37] A. J. Hadi, U. M. Nayef, F. A.-H. Mutlak, and M. S. Jabir, "High-Efficiency Photodetectors Based on Zinc Oxide Nanostructures on Porous Silicon Grown by Pulsed Laser Deposition," *Plasmonics*, vol. 19, no. 2, pp. 577–593, Apr. 2024.